

No evidence for p - or d -wave dark matter annihilation from local large-scale structure

A. Kostić,^{1,*} D. J. Bartlett,^{2,3,†} and H. Desmond⁴

¹*Max Planck Institute for Astrophysics, Karl-Schwarzschild-Straße 1, 85748 Garching, Germany*

²*CNRS & Sorbonne Université, Institut d'Astrophysique de Paris (IAP),*

UMR 7095, 98 bis bd Arago, F-75014 Paris, France

³*Astrophysics, University of Oxford, Denys Wilkinson Building, Keble Road, Oxford, OX1 3RH, UK*

⁴*Institute of Cosmology & Gravitation, University of Portsmouth,*

Dennis Sciama Building, Portsmouth, PO1 3FX, UK

If dark matter annihilates into standard model particles with a cross-section which is velocity dependent, then Local Group dwarf galaxies will not be the best place to search for the resulting gamma ray emission. A greater flux would be produced by more distant and massive halos, with larger velocity dispersions. We construct full-sky predictions for the gamma-ray emission from galaxy- and cluster-mass halos within ~ 200 Mpc using a suite of constrained N -body simulations (CSiBORG) based on the Bayesian Origin Reconstruction from Galaxies algorithm. Comparing to observations from the *Fermi* Large Area Telescope and marginalising over reconstruction uncertainties and other astrophysical contributions to the flux, we obtain constraints on the cross-section which are two (seven) orders of magnitude tighter than those obtained from dwarf spheroidals for p -wave (d -wave) annihilation. We find no evidence for either type of annihilation from dark matter particles with masses in the range $m_\chi = 2 - 500$ GeV/ c^2 , for any channel. As an example, for annihilations producing bottom quarks with $m_\chi = 10$ GeV/ c^2 , we find $a_1 < 2.4 \times 10^{-21}$ cm³s⁻¹ and $a_2 < 3.0 \times 10^{-18}$ cm³s⁻¹ at 95% confidence, where the product of the cross-section, σ , and relative particle velocity, v , is given by $\sigma v = a_\ell (v/c)^{2\ell}$ and $\ell = 1, 2$ for p -, d -wave annihilation, respectively. Our bounds, although failing to exclude the thermal relic cross-section for velocity-dependent annihilation channels, are among the tightest to date.

I. INTRODUCTION

An unambiguous detection of non-gravitational interactions of dark matter continues to evade us. Astrophysical objects are ideal targets in the search for novel dark matter physics, since low interaction rates can be compensated by the large quantities of dark matter, leading to potentially detectable signals. For over a decade, the origin of the observed excess of gamma rays at the centre of our galaxy – known as the Galactic Centre Excess (GCE) [1–3] – has been debated, with explanations such as unresolved point sources or dark matter annihilation being proposed [e.g. 4–30]. The majority of work on this excess has focused on s -wave annihilation, where the product of the self-annihilation cross-section, σ , and relative velocity, v , is independent of v . Such models can be strongly constrained by considering the gamma ray flux from nearby dwarf galaxies [31–33], which are able to rule out the thermal relic cross-section for dark matter particle masses relevant to explain the GCE.

Not all dark matter annihilation models require σv to be independent of velocity. For example, for fermionic dark matter annihilation to spin-0 particles, even parity final states cannot have an s -wave contribution in parity conserving theories [34, 35]. p -wave annihilation – where σv is proportional to the square of the relative velocity – dominates when Standard Model fermion-antifermion pairs are produced from Majorana fermions in models

with minimal flavour violation due to chirality suppression of s -wave annihilation [36]. If dark matter is instead a real scalar, then d -wave annihilation – where the fourth power of the relative velocity is relevant – is dominant [37, 38].

If the GCE were due to velocity-dependent dark matter annihilation, then, despite their close proximity, dwarf spheroidals cannot provide tight constraints on the annihilation cross-section, since the low velocity dispersions in these objects result in heavily suppressed annihilation rates. One should therefore test whether these velocity-dependent models are compatible with other observations of gamma ray fluxes, since these can evade bounds from these objects. In these scenarios, one would expect a large signal from extra-galactic halos, where the velocity dispersion should be larger. It has therefore been recently suggested to use extra-galactic halos to search for velocity-dependent dark matter annihilation signals in gamma ray data [39].

In this paper we perform this test for p -wave and d -wave annihilation, where the cross-section is proportional to the square and fourth power of the relative velocity between dark matter particles, respectively. As in our previous work constraining s -wave annihilation [40], we utilise the CSiBORG [41–43] suite of constrained N -body simulations to produce full-sky templates for the dark matter annihilation flux, which are then compared to the observations of the *Fermi* Large Area Telescope via a Markov Chain Monte Carlo (MCMC) algorithm. The initial conditions for these simulations are inferred using the BORG (Bayesian Origin Reconstruction from Galaxies) algorithm and are designed to produce three-

* akostic@mpa-garching.mpg.de

† deaglan.bartlett@iap.fr

dimensional dark matter density fields which match the observed positions of galaxies in the 2M++ galaxy catalogue [44, 45]. We marginalise over uncertainties in this reconstruction as well as over non-dark-matter contributions to the gamma ray sky. Our constraints on the self-annihilation cross-section are two (seven) orders of magnitude tighter than those obtained using dwarf spheroidal galaxies for p -wave (d -wave) annihilation.

In Section II we describe how we forward model the dark matter annihilation flux, discuss the models used for competing astrophysical contributions to the signal, and outline our inference procedure. These predictions are compared to observations, presented and discussed in Sections III and IV, and we conclude in Section V.

II. METHODS

A. Bayesian large-scale structure inference

In this work we study the expected gamma ray flux from dark matter annihilation in extragalactic halos. To determine the masses and locations of these halos, we use the CSiBORG suite of 101 dark matter-only constrained simulations [41–43]. The initial conditions of these simulations produce present-day density fields which match the observed number densities of galaxies in the 2M++ galaxy compilation [44, 45] and are inferred using the BORG algorithm [see e.g. 44, 46–49]. This algorithm produces a Markov Chain of plausible initial conditions via the application of a Bayesian forward model and marginalises over galaxy bias parameters. The initial conditions are constrained in a box of length $677.7h^{-1}$ Mpc with 256^3 voxels. For each CSiBORG simulation these initial conditions are augmented with white noise to a resolution of 2048^3 within $155h^{-1}$ Mpc of the Milky Way (giving a mass resolution of $4.4 \times 10^9 M_\odot$) and run to $z = 0$ using RAMSES [50]. The watershed halofinder PHEW [51] is applied on-the-fly to the dark matter particles with the standard threshold of $200\rho_c$. We do not consider sub-halos and the minimum halo mass used (M_{200m}) is $4.4 \times 10^{11} M_\odot$. The resulting halo catalogues are publicly available at [52].

B. Velocity-dependent J factor

In this work we consider dark matter annihilation of particles of mass m_χ , with a cross-section σ which depends on the relative velocity, v , between annihilating dark matter particles as

$$\sigma v = a_\ell S_\ell \left(\frac{v}{c} \right), \quad (1)$$

where a_ℓ is a constant and S_ℓ can be an arbitrary function of v/c . At observed energy E_γ , the differential photon

flux, $d\Phi_\gamma/dE_\gamma$, is

$$\frac{d\Phi_\gamma}{dE_\gamma} = \frac{a_\ell}{8\pi m_\chi^2} J^\ell \sum_i \text{Br}_i \left. \frac{dN_i}{dE'_\gamma} \right|_{E'_\gamma = E_\gamma(1+z)}, \quad (2)$$

where we sum over annihilation channels with branching ratios Br_i . This equation is valid if dark matter is entirely comprised of a single particle whose antiparticle is itself. We introduced the J factor

$$J_{\mu,p}^\ell = \int_{\mu,p} d\Omega d\mu d^3v_1 d^3v_2 S_\ell \left(\frac{|\mathbf{v}_1 - \mathbf{v}_2|}{c} \right) \times f(\mathbf{r}(\mu), \mathbf{v}_1) f(\mathbf{r}(\mu), \mathbf{v}_2), \quad (3)$$

where $f(\mathbf{r}(\mu), \mathbf{v})$ is the distribution function of DM particles, which we integrate over the velocities of the two particles, \mathbf{v}_1 and \mathbf{v}_2 , and along the line of sight coordinate, μ . Since we define these quantities on a discretised map, we also integrate across the HEALPIX¹ pixel area p . For simplicity, we assume that the decays occur via one channel, so the branching ratio, Br_i is either 0 or 1. Note that the photon distribution function, dN_i/dE'_γ should be evaluated at the redshift of the halo. Since we will be using low-redshift halos in this work ($z \lesssim 0.05$) we will neglect this redshift effect and thus assume that $E'_\gamma \approx E_\gamma$. Introducing redshift dependence would require inserting a redshift dependent optical depth into Eq. (2), which, in our case, will only marginally affect the results (see for example the discussion in Section IV.B.5 in [40]).

In this work we will consider p -wave and d -wave annihilation, i.e. $S_\ell(x) = x^{2\ell}$, where $\ell = 1$ (p -wave) or $\ell = 2$ (d -wave). In the following two sections we describe how one can obtain the J factor for these models from the density profile of a dark matter halo.

1. J factor for p -wave annihilation

For p -wave annihilation, the J factor can be re-written as

$$\begin{aligned} J_{\mu,p}^{(\ell=1)} &= 2 \int_{\mu,p} d\Omega d\mu \rho^2(\mathbf{r}(\mu)) \left\langle \frac{\mathbf{v}^2}{c^2} \right\rangle(\mathbf{r}(\mu)) \\ &= \frac{2}{c^2} \int_{\mu,p} d\Omega d\mu \rho^2(\mathbf{r}(\mu)) (\sigma_r^2(\mathbf{r}(\mu)) + 2\sigma_\theta^2(\mathbf{r}(\mu))), \end{aligned} \quad (4)$$

where $\rho(\mathbf{r}(\mu))$ is the dark matter density at the position μ along the line of sight and σ_r and σ_θ are the corresponding radial and tangential velocity dispersion, respectively. We keep the explicit dependence on the line of sight position in order to emphasize that the J factor needs to be evaluated with respect to the observer. However, since

¹ <http://healpix.sf.net>

the total J factor within a pixel is a scalar quantity, one can also first evaluate it within the corresponding volume with respect to the halo centre and then make the appropriate projection. This is precisely how the CLUMPY package – which we utilise here – works (see [40, 53–55]). Now, to obtain the dispersion for a given halo, we assume spherical symmetry, and therefore must solve the Jeans equation

$$\frac{1}{\rho} \frac{d}{dr} (\rho \sigma_r^2) + 2\beta \frac{\sigma_r^2}{r} = -\frac{d\Phi}{dr}, \quad (5)$$

where we introduce an anisotropy parameter

$$\beta(r) = 1 - \frac{\sigma_\theta^2(r)}{\sigma_r^2(r)}, \quad (6)$$

and Φ is the gravitational potential of the halo.

We assume that all our halos have Navarro-Frenk-White (NFW) [56] density profiles

$$\rho(r) = \frac{\rho_0}{r/r_s (1 + r/r_s)^2}, \quad (7)$$

with scale length r_s , defined such that the concentration of the halo is $c = r_{\text{vir}}/r_s$ for virial radius r_{vir} . In this work we use the mean mass-concentration relation of Prada *et al.* [57], Sánchez-Conde and Prada [58] and assume zero scatter in this relation. Since the J factor traces the square of the density, one may expect that subhalos or clumps may provide a significant contribution to the J factor and should also be included. Although this is true for s -wave annihilation, the small velocity dispersion of these clumps means that the overall signal is dominated by the smooth component and we therefore ignore unresolved substructure. This approximation has been validated by explicitly calculating the J factor for halos from hydrodynamical simulations [59], although we note that this conclusion does not hold for the case of Sommerfeld enhanced annihilation (see for example [60, 61]). We do not consider this case in this paper and leave it for future work.

Defining the dimensionless radial coordinate $s \equiv r/r_{\text{vir}}$, one finds that the radial velocity dispersion for circular orbits is (see Eq. (14) in [62])

$$\begin{aligned} \frac{\sigma_r^2}{V_{\text{vir}}^2}(s) \stackrel{\beta=0}{=} & \frac{c^2 s (1+cs)^2}{2(\ln(1+c) - c/(1+c))} \left[\pi^2 + 6 \text{Li}_2(-cs) \right. \\ & - \ln(cs) + \left(1 + \frac{1}{c^2 s^2} - \frac{4}{cs} - \frac{2}{1+cs} \right) \times \ln(1+cs) \\ & \left. + 3 \ln^2(1+cs) - \frac{1}{cs} - \frac{6}{1+cs} - \frac{1}{(1+cs)^2} \right], \end{aligned} \quad (8)$$

where V_{vir} is the virial velocity, and Li_2 is the dilogarithm function. Similarly, for the extreme cases of a constant anisotropy parameter $\beta = 0.5$ and $\beta = 1.0$ one finds (see

Eq. (15) and (16) from [62])

$$\begin{aligned} \frac{\sigma_r^2}{V_{\text{vir}}^2}(s) \stackrel{\beta=0.5}{=} & \frac{c(1+cs)^2}{(\ln(1+c) - c/(1+c))} \left[-\frac{\pi^2}{3} - 2 \text{Li}_2(-cs) \right. \\ & + \frac{2}{1+cs} + \frac{\ln(1+cs)}{cs} + \frac{\ln(1+cs)}{1+cs} \\ & \left. - \ln^2(1+cs) - \frac{1}{2(1+cs)^2} \right], \\ \frac{\sigma_r^2}{V_{\text{vir}}^2}(s) \stackrel{\beta=1}{=} & \frac{(1+cs)^2}{s(\ln(1+c) - c/(1+c))} \left[\frac{\pi^2}{6} + \text{Li}_2(-cs) \right. \\ & \left. - \frac{1}{1+cs} - \frac{\ln(1+cs)}{1+cs} + \frac{\ln^2(1+cs)}{2} \right]. \end{aligned} \quad (9)$$

In Fig. 1 we show how these different velocity dispersion profiles affect the angular dependence of the normalised J factor (labelled as \tilde{J}) for a halo of mass $M = 1.2 \times 10^{15} M_\odot$ (one of the most massive halos in CSiBORG simulation 9844) at a distance of ~ 100 Mpc from the observer. The quantity \tilde{J} we calculate as

$$\tilde{J}^\ell(\theta) = \frac{J^\ell(\theta)}{\int d\Omega J^\ell(\theta)}, \quad (10)$$

where θ is the angular distance from the halo centre as seen on the sky. We perform this calculation from close to the halo centre, $\theta \sim 0.01^\circ$, all the way up to the two times the virial radius of the halo. Similar results for the case of the Milky Way halo (modelled as a NFW profile) were obtained through the Eddington inversion method in [63]. We show the results for p -wave with different values of the anisotropy parameter β (Eqs. (8) and (9)) and d -wave calculations. The $\beta = 0.5$ (dashed) and $\beta = 1.0$ (dotted-dashed) cases are more strongly peaked at the centre than the corresponding $\beta = 0$ case, reflecting the behaviour of the velocity dispersion profiles (see also Fig. 1 in [62]). Furthermore, for $\beta = 1.0$, \tilde{J} diverges at the centre and hence needs to be regularised (see Eq. (20)). The d -wave \tilde{J} shows qualitatively similar behaviour as the corresponding p -wave case (thick line). For more details on the d -wave calculation, see Section II B 2 and Appendix A.

It should be noted that, for a more realistic scenario, the anisotropy parameter should be taken as a radially varying function (see [64–66]). We do not consider these models here, given that the three extreme scenarios for the anisotropy parameter we pick should bracket reality. In our fiducial analysis we choose $\beta = 0$, however, and show in Section IV B 1 that this is a conservative choice. The corresponding J factor calculation then simply consists of substituting Eq. (8) into Eq. (4), noting that in this case $\sigma_\theta = \sigma_r$, and integrating the final expression for all our halos. We do this numerically using the CLUMPY package at a HEALPIX resolution of $\text{nside} = 2048$, which is then subsequently degraded to the coarser resolution ($\text{nside} = 256$) at which we perform the inference. This allows a more faithful calculation of the J factor

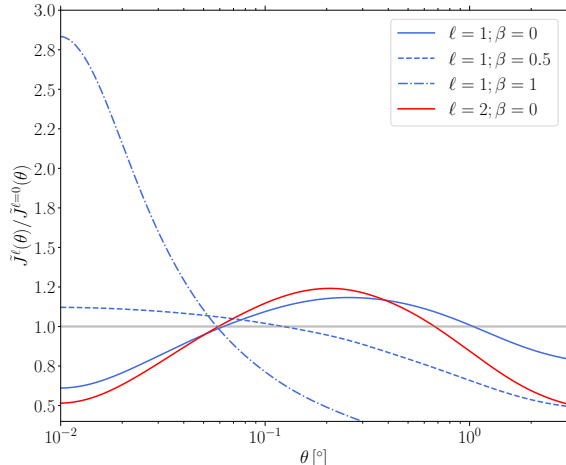


FIG. 1. The angular distribution of the normalised J factor, \tilde{J} (Eq. 10), as a function of angle on the sky from the halo centre, θ , for p -wave ($\ell = 1$) and d -wave ($\ell = 2$) annihilation channels. The results are shown relative to the s -wave ($\ell = 0$) result and for different choices of anisotropy parameter, β . For this example, we used one of the most massive halos from the CSIBORG 9844 realisation with $M = 1.2 \times 10^{15} M_{\odot}$ at a distance of 96 Mpc from the observer.

than performing the calculation at `nside = 256`, since the dependence of J on ρ is non-linear.

2. J factor for d -wave annihilation

For d -wave annihilation the corresponding expression for the J factor takes the form (see also [67])

$$J_{\mu,p}^{(\ell=2)} = \int_{\mu,p} d\Omega d\mu \rho^2(\mathbf{r}) \left(2 \left\langle \frac{\mathbf{v}^4}{c^4} \right\rangle(\mathbf{r}) + \frac{10}{3} \left\langle \frac{\mathbf{v}^2}{c^2} \right\rangle^2(\mathbf{r}) \right). \quad (11)$$

We see that the second term appearing can be computed from a power of the velocity dispersion (as in p -wave; see Eq. (4)), but the first term requires the evaluation of the fourth moment of the velocity distribution. In general, this would require for solving the Boltzmann hierarchy up to the fourth moment. It will not be possible to do so, however, since this system of equations is not closed for a general self-gravitating stellar system. In order to solve the Jeans system of differential equations, one must impose additional constraints. This can be done by requiring the stellar system has certain symmetries. One of the possibilities is to assume an ergodic distribution function ($\beta = 0$, see Section 4 - Box 4.3 of [68]). This then allows to write down the following equation, relating $\langle v_r^2 \rangle$ and $\langle v_r^4 \rangle$

$$\frac{d}{dr} (\rho \langle v_r^4 \rangle) \stackrel{\beta=0}{=} -3\rho \langle v_r^2 \rangle \frac{d\Phi}{dr}, \quad (12)$$

where by v_r we have denoted the projection of the velocity to the radial direction (fixing the coordinate system to the halo centre of mass). In addition to calculating $\langle v_r^4 \rangle$, we need to also calculate the other projected moments as well as the cross-terms in order to obtain the total fourth moment of the velocity, as is necessary for evaluating the Eq. (11). This is straightforward, due to the ergodicity of the distribution function, as shown in Appendix A. The final expression for the fourth velocity moment is then given by

$$\langle \mathbf{v}^4 \rangle \stackrel{\beta=0}{=} 5 \langle v_r^4 \rangle. \quad (13)$$

This, and the solution for $\langle \mathbf{v}^2 \rangle$ from Eq. (8), are then enough to evaluate the total J factor for d -wave annihilation. See Appendix A for more details.

C. Gamma ray data

We compare the dark matter annihilation templates to the gamma ray observations from *Fermi* Large Area Telescope between mission weeks 9 and 634. We select photons in the upper quartile of angular resolution (PS3) and event class SOURCEVETO in the energy range 500 MeV – 50 GeV. The maximum zenith angle is chosen to be 90° . These are binned spatially onto HEALPIX [69, 70] maps with resolution `nside = 256` and into 9 logarithmically spaced energy bins. The processing of the photon files is performed using the *Fermi* Tools² and FERMIPY [71]. We also use this software to convolve our templates with the *Fermi* point spread function and to obtain the exposure maps. To reduce the impact of galactic emission and the GCE, we mask the region with galactic latitude $|\lambda| < 30^\circ$.

Although some of the photons detected by *Fermi* could have been produced by dark matter annihilation, there are other sources which will also contribute, and thus it is important to incorporate these in the analysis. As in our previous work [40], we consider three contributions: point sources (psc), an isotropic background (iso) and the Milky Way (gal). Each contribution is modelled with a fixed spatial template for energy bin i , $\{T_i^t(\hat{r}) : t \in \{\text{iso}, \text{gal}, \text{psc}\}\}$, where we assign a different normalisation, A_i^t , for each energy bin and template. We jointly infer these parameters with the amplitude of the J factor template. The point source template is comprised of all extended and point sources in the Large Area Telescope 12-year Source Catalog (4FGL-DR3)³ and the galactic component is modelled using the templates described in [72]. The scalings $\{A_i^t\}$ are defined such that they all equal unity if the *Fermi* data is perfectly described by these templates, however jointly in-

² <https://fermi.gsfc.nasa.gov/ssc/data/analysis/software/>

³ <https://heasarc.gsfc.nasa.gov/W3Browse/fermi/fermilpsc.html>

ferring these parameters will allow us to capture any imperfections in the spectral modelling. We thus require an initial guess for the isotropic component's spectral shape, for which we use the *Fermi* Isotropic Spectral Template⁴. All templates are convolved with the *Fermi* point spread function using the Fermi Tools.

D. Likelihood model

As in [40], we constrain the dark matter annihilation cross-section in two steps. First, we do not assume a functional form for the spectrum, but infer the normalisation of each template in each energy bin for each CSiBORG simulation separately. We then fit this inferred spectrum to a functional form in the second step, which allows us to constrain a_ℓ .

For pixel p and CSiBORG simulation j , the mean number of counts in energy bin i is predicted to be

$$\lambda_{ipj} = \mathcal{F}_{ip} \times \left(A_i^J J_{ipj} + \sum_t A_i^t T_{ip}^t \right), \quad (14)$$

where the \mathcal{F}_{ip} is the *Fermi* exposure, and we have defined

$$J_{ipj} \equiv \frac{J_{pj}}{J_0} \Delta E_i, \quad T_{ip}^t \equiv \int_p T_i^t(\hat{r}) d\Omega, \quad (15)$$

where $J_0 = 10^{13} \text{ GeV}^2 \text{ cm}^{-5}$ sets the units. We assume that the photon counts are Poisson distributed, such that the likelihood for observing n_{ip} counts in pixel p and energy bin i given the mean λ_{ipj} is

$$\mathcal{L}(n_{ip} | \lambda_{ipj}) = \frac{\lambda_{ipj}^{n_{ip}} \exp(-\lambda_{ipj})}{n_{ip}!}. \quad (16)$$

Given this likelihood, we then apply Bayes' identity

$$\begin{aligned} \mathcal{P}(A_i^J, \{A_i^t\}, j | \mathcal{D}_i) \\ = \frac{\mathcal{L}(\mathcal{D}_i | A_i^J, \{A_i^t\}, j) P(A_i^J) P(\{A_i^t\}) P(j)}{\mathcal{Z}(\mathcal{D}_i)}, \end{aligned} \quad (17)$$

to obtain the posterior distribution for the model parameters, \mathcal{P} , where \mathcal{Z} is the evidence. For our priors, P , we enforce the improper, uniform priors $a_\ell, A_i^J \geq 0$, and a uniform prior on our non-dark matter templates, A_i^t , between 0.5 and 1.5, where $A_i^t \in \{A_i^{\text{gal}}, A_i^{\text{iso}}, A_i^{\text{psc}}\}$. We run the No U-Turn Sampler implemented in NUMPYRO [73, 74] for 5000 steps after an initial 1000 warmup steps. We find this typically leads to at least $\mathcal{O}(2000)$ effective samples in all parameters, and Gelman-Rubin statistics consistent with unity within 10^{-2} .

We then marginalise over all other parameters and average over the $N_{\text{sim}} = 101$ CSiBORG realisations, assigning them equal weights, to obtain the one-dimensional posterior for the annihilation flux in a given energy bin

$$\mathcal{P}(A_i^J | \mathcal{D}_i) = \frac{1}{N_{\text{sim}}} \sum_j \int d\{A_i^t\} \mathcal{P}(A_i^J, \{A_i^t\}, j | \mathcal{D}_i). \quad (18)$$

Assuming a given annihilation channel and particle mass, and that each energy bin is independent, the set of A_i^J can be trivially utilised to constrain a_ℓ by evaluating the predicted A_i^J for the model and multiplying the resultant probabilities. We use the pre-computed spectra calculated by Jeltima and Profumo [75] and provided by the *Fermi* collaboration⁵ which capture the energy spectra of intermediately produced standard model particles and their final products.

III. RESULTS

The first step of our inference infers the amplitudes of the J factor templates, A_i^J , for each energy bin, i . In Fig. 2 we plot the one-dimensional posterior distributions of these parameters and see that these coefficients are consistent with zero at 1σ confidence for all energy bins for both p - and d -wave annihilation. In the second step we fit this inferred spectrum to a dark matter annihilation model and hence can constrain a_ℓ . For reference, in Fig. 2 we plot example spectra for annihilation via the $b\bar{b}$ channel for $m_\chi = 100 \text{ GeV}/c^2$ at a fiducial a_ℓ .

In Fig. 3 we convert these posteriors to 95% upper limits on the p - and d -wave self-annihilation cross-section ($\sigma v = a_\ell (v/c)^{2\ell}$) as a function of dark matter particle mass, m_χ , for the production of any standard-model quark, charged lepton or gauge boson (except photons). We do not attempt to constrain m_χ , and instead find constraints on a_ℓ conditioned on this variable for the range $m_\chi \in [2, 500] \text{ GeV}/c^2$. In all cases we find no evidence for p -wave or d -wave dark matter annihilation, as all the fluxes in Fig. 2 are consistent with zero. For dark matter annihilating to $b\bar{b}$, if $m_\chi = 10 \text{ GeV}/c^2$, we constrain $a_1 < 2.4 \times 10^{-21} \text{ cm}^3 \text{ s}^{-1}$ and $a_2 < 3.0 \times 10^{-18} \text{ cm}^3 \text{ s}^{-1}$ at 95% confidence. For an annihilation which forms lighter quarks, we obtain practically identical constraints, whereas lepton production yields constraints which are approximately an order of magnitude less stringent. For large $m_\chi \gtrsim 100 \text{ GeV}/c^2$, our upper limits for the production of top quarks or W or Z bosons are similar to those for lighter quarks, but these processes cannot occur at lower m_χ so we do not obtain constraints for smaller dark matter particle masses.

Note that, in Fig. 3, the constraints weaken as m_χ approaches m_A , if the annihilation product is $A\bar{A}$. Near

⁴ <https://fermi.gsfc.nasa.gov/ssc/data/access/lat/BackgroundModels.html>

⁵ https://fermi.gsfc.nasa.gov/ssc/data/analysis/scitools/source_models.html

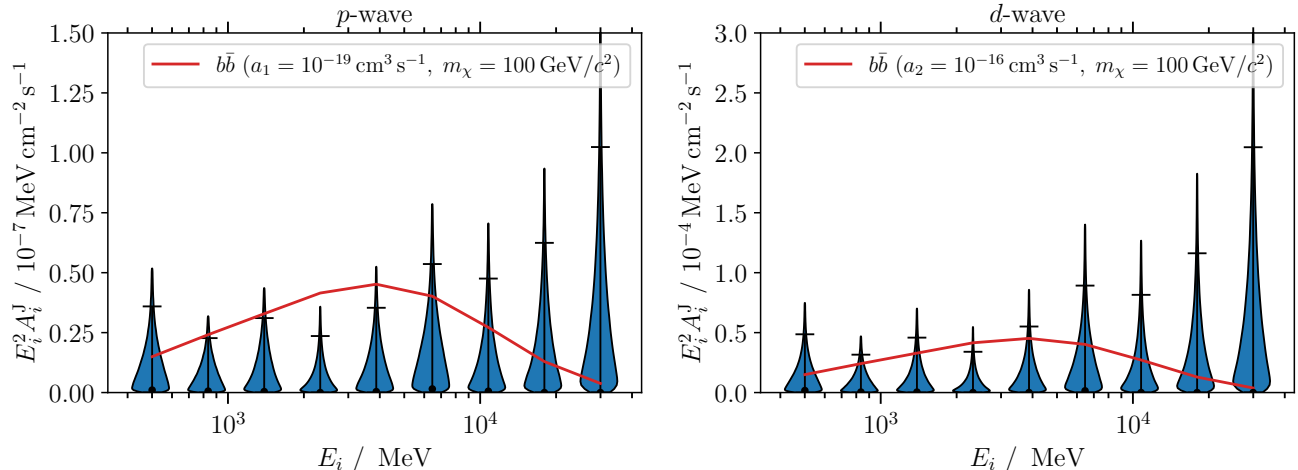


FIG. 2. Posterior distributions of the amplitudes of the J factor templates for each energy bin, i , for p -wave (left) and d -wave (right) annihilation. The black points are the maximum posterior points and the error bars indicate the 1σ confidence intervals. For reference we also plot the expected A_i^J for dark matter annihilation via the $b\bar{b}$ channel for dark matter particles of mass $m_\chi = 100 \text{ GeV}/c^2$, with $a_1 = 10^{-19} \text{ cm}^3 \text{ s}^{-1}$ (p -wave) and $a_2 = 10^{-16} \text{ cm}^3 \text{ s}^{-1}$ (d -wave). All fluxes are consistent with zero, indicating no detection of dark matter p -wave or d -wave annihilation.

this value, the process is strongly suppressed and hence the constraints no longer lie within the range of the plot, so we do not plot these points.

For comparison, for p -wave, in Fig. 3 we also plot the constraints one obtains for the $b\bar{b}$ channel from dwarf spheroidals. As anticipated from the much smaller velocity dispersion in dwarf galaxies, our constraints are significantly tighter, by approximately two orders of magnitude for p -wave annihilation, and seven orders of magnitude for d -wave. This demonstrates the increased importance of large halo masses for velocity-dependent annihilation, whereas for s -wave annihilation the close proximity of these objects more than compensates for their small masses, leading to tighter constraints [see e.g. Figure 7 of 40]. We perform a more detailed comparison to the literature in Section IV D.

IV. DISCUSSION

A. Understanding the results

To determine which halos are responsible for our constraints, we produce J factor maps for halos only within a given mass range and run the inference using only those halos. For computational convenience, we perform this on one representative CSiBORG simulation only (9844). The results of this inference are plotted in Fig. 4, where we use moving mass bins of width $\Delta \log_{10}(M_h/M_\odot) = 1$ and consider dark matter particles of mass $m_\chi = 8 \text{ GeV}/c^2$ annihilating via the $b\bar{b}$ or e^+e^- channels. We see that our constraints are dominated by the most massive objects in our simulations, i.e. halos of

mass $M_h \sim 10^{14-16} M_\odot$. This is due to both the larger densities and velocity dispersions in massive objects, as was predicted by Baxter *et al.* [39] (see their Fig. 3). If we continued Fig. 4 to larger M_h we would see that the constraints would begin to weaken, due to the lack of very massive objects in our simulation. We observe that the constraining power as a function of mass for p -wave annihilation plateaus at an earlier halo mass than for d -wave annihilation due to the weaker dependence on the relative velocity between dark matter particles, which increases with mass. Qualitatively similar results are seen for other channels and dark matter particle masses. Again, this is consistent with the expectations of Baxter *et al.* [39]. We find that the total J factors we obtained, for the 128 most massive halos of one of our CSiBORG realisation (9844), agree to within factor of ~ 5 when compared to the expression in Eq. (3.3) of [39]. This is a consequence of more detailed modelling of the J -factor in this work; for example, if Baxter *et al.* [39] chose a different mass definition, given the strong dependence of the p - and d -wave annihilation channels on total mass of the object, this difference could be alleviated.

To assess which energy bins drive our constraints, for each channel and m_χ we calculate the log-likelihood at the 95% upper limit on a_ℓ for each energy bin and compare to the values for $a_\ell = 0$. For both p - and d -wave annihilation, we find that the first three energy bins are the most constraining for $m_\chi \lesssim 30 \text{ GeV}/c^2$, whereas the fourth energy bin becomes particularly important for higher masses. This is the same behaviour as for s -wave annihilation [40], which is attributed to the lower expected photon counts in the higher energy bins, and therefore weaker constraining power. As one increases

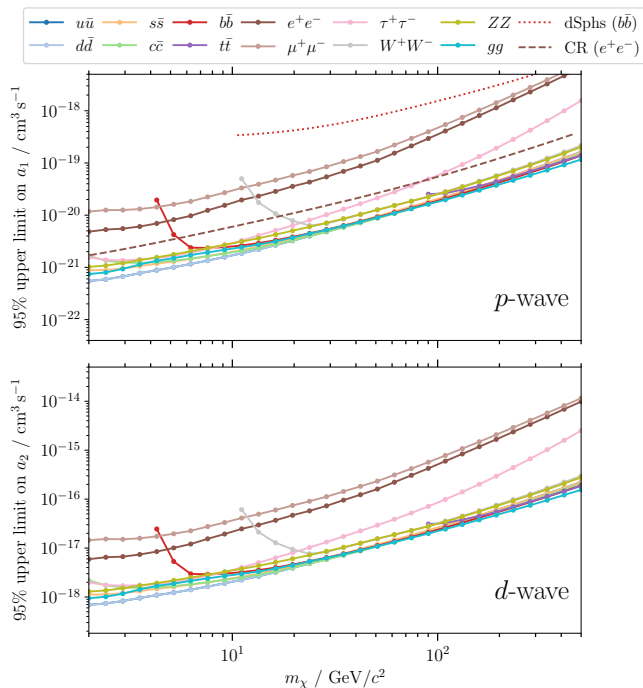


FIG. 3. 95% upper limit on the dark matter p -wave (upper, $\ell = 1$) and d -wave (lower, $\ell = 2$) annihilation cross-section parameter, a_ℓ , where the annihilation cross-section is $\sigma v = a_\ell (v/c)^{2\ell}$. The solid lines and points are from this work. Each constraint is derived at a fixed dark matter particle mass m_χ as indicated on the x -axis. The red dotted line is a constraint obtained from dwarf spheroidal (dSph) satellites of the Milky Way [76, 77] for the $b\bar{b}$ channel. We find that our constraints are approximately two orders of magnitude tighter than those from dSphs due to the larger velocity dispersions in massive extragalactic halos. The dSph constraint for d -wave is off the top of the plot. The brown dashed line is the constraint for the e^+e^- channel, directly detecting the resulting electrons and positrons, assuming they are produced by the galactic halo [78]. This is slightly tighter than our e^+e^- constraint.

m_χ , one expects more photons at higher energy, and thus the relative importance of these bins increases.

B. Systematic uncertainties

1. J factor calculation

In Equation (18) we marginalised over uncertainties in the large-scale density modes which are constrained from the BORG algorithm, as well as smaller-scale unconstrained modes which were added as white noise in the initial conditions. In our fiducial analysis we use the full suite of 101 CSiBORG simulations, however to verify this is a sufficiently large number, we rerun our analysis one hundred times using fifty randomly selected CSiBORG simulations (with repeats) each time. This yields an uncertainty on the 95% upper limit of a_ℓ of no more than

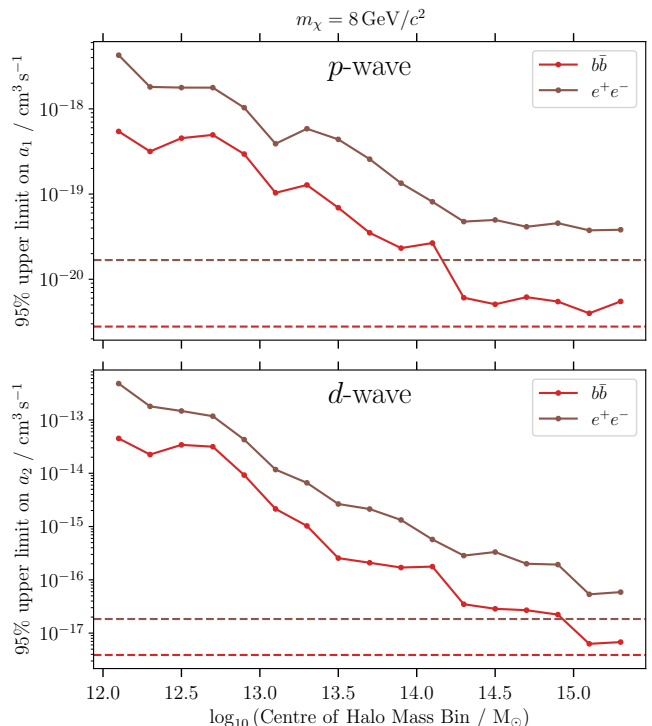


FIG. 4. Constraints on p -wave (upper, $\ell = 1$) and d -wave (lower, $\ell = 2$) annihilation cross-section, $\sigma v = a_\ell (v/c)^{2\ell}$, from halos in a given mass range from a single CSiBORG simulation (9844). Each mass bin has a width $\Delta \log_{10}(M_h/M_\odot) = 1$, and we use a sliding window. We plot the 95% upper limits on a_ℓ for the $b\bar{b}$ and e^+e^- channels; the dashed horizontal lines are the constraints obtained from all halos together. We see that our constraints are driven by the most massive halos and that this is more important for d -wave annihilation due to the stronger dependence of annihilation rate on the relative velocity between dark matter particles.

5.9% and 6.5% for p -wave and d -wave annihilation, respectively, when considering all channels and particle masses separately. The median change in the constraint across these runs at a given mass and channel changes by no more than 1.2% compared to the fiducial analysis. Thus, we conclude that this is an appropriate number of simulations.

For our p -wave analysis, we assumed circular orbits for dark matter particles ($\beta = 0$), leading to the radial velocity dispersion given in Eq. (8). Similar expressions exist for alternative values of β , thus to determine the impact of this assumption on our constraints, we compute J factor maps assuming $\beta = 0.5$ or $\beta = 1$ (although the latter case is unrealistic as this corresponds to purely radial orbits) for a representative CSiBORG simulation (9844) and rerun our analysis to obtain alternative constraints on a_1 .

For $\beta = 1$, one finds that the J factor diverges logarithmically towards the centre, and thus simply computing Eq. (4) would predict an infinite annihilation flux from each halo. In practice, if the annihilation rate becomes

sufficiently high, then it will disrupt the density profile of the halo as the dark matter particles will be depleted towards the centre, presumably forming a cored profile. Thus, Eq. (4) is only valid up to some core radius, r_c . We estimate this to be the radius at which the dynamical time scale of the halo ($1/\sqrt{G\rho}$) equals the annihilation time scale ($\rho\sigma v/m_\chi$). Since we expect this to occur close to the centre of the halo, we use the leading order term for σ_r^2 ,

$$\frac{\sigma_r^2}{V_{\text{vir}}^2} \stackrel{\beta=1}{=} \frac{\pi^2 - 9}{6 \left(\log(1+c) - \frac{c}{1+c} \right)} \frac{1}{s} + \mathcal{O}(s^0), \quad (19)$$

and assume $\rho \sim \rho_0 r_s/r$ (see Eq. (7)). This leads to a core radius of

$$r_c \sim \left(\frac{\pi^2 - 9}{6} \frac{a_1}{m_\chi} \frac{V_{\text{vir}}^2}{\log(1+c) - \frac{c}{1+c}} \sqrt{\frac{\rho_0}{G}} \right)^{\frac{2}{3}} r_{\text{vir}}. \quad (20)$$

We have verified that, for the core radii that this implies, the $\mathcal{O}(s^0)$ term is negligible compared to the leading order term.

For simplicity, we compute Eq. (4) using r_c as the lower limit of the integral and add the contribution from the cored region separately. Furthermore, we note that Eq. (20) depends on a_1 and m_χ , and thus a fully-consistent analysis should recompute the J factor at each step in the MCMC and for each channel. However, this is computationally infeasible. Instead, we set $a_1 = 2.4 \times 10^{-21} \text{ cm}^3 \text{ s}^{-1}$ and $m_\chi = 100 \text{ GeV}/c^2$ in this formula; this is a characteristic WIMP mass with a_1 at approximately the 20th percentile for the $b\bar{b}$ channel when $\beta = 0.5$. This typically leads to a core radius of $r_c \sim 0.1 - 1 \text{ pc}$. We find that the constraints on a_1 for $\beta = 1$ are much tighter than this, and thus our approximation yields a conservative constraint.

For both $\beta = 0.5$ and $\beta = 1$, we find that the anisotropic J factors lead to tighter constraints for all masses and channels, by up to a factor of 2.3 for $\beta = 0.5$ and up to two orders of magnitude for $\beta = 1$. This simply reflects the general behaviour of the J factor for these two different anisotropic profiles. As can be seen from Fig. 1, the $\beta = 0.5$ and $\beta = 1.0$ profiles are more strongly peaked towards the centre than the corresponding $\beta = 0$ case, with $\beta = 1.0$ diverging more quickly towards the centre and giving total J factors between 50 – 100 times larger than the corresponding $\beta = 0$ case. From this and Eq. (2), it is then easy to see that the derived constraints for these respective cases will show similar trends. Choosing $\beta = 0$ is therefore the most conservative of the cases considered, justifying our use of it in our fiducial analysis.

For all halos considered in this work, we have not attempted to add corrections to the halo density profiles due to baryonic effects, and have instead used profiles calibrated against dark-matter-only simulations. In the presence of baryons, adiabatic contraction during galaxy formation [79, 80] can steepen the central density profile,

or it can be made shallower due to the subsequent stellar feedback [81, 82]. The different resulting density profiles would change our J factor calculations and hence our constraints on a_ℓ . Indeed, cosmological zoom hydrodynamical simulations have demonstrated that baryons do affect the J factors for velocity-dependent annihilation, typically increasing J from a factor of a few up to factors of several hundred [83, 84]. Assuming this increase in J can be applied to our halos, then our constraints on a_ℓ are conservative, however we leave it to future work to implement more precise corrections for baryonic physics.

2. Constrained simulation volume

As already argued in Section VI.B.5 of [40], the choice of HEALPIX `nside=256` for our inference pipeline allows for circumventing the issue of the limited volume we have for our CSiBORG simulation suite ($z \lesssim 0.05$). This is because any sources beyond the CSiBORG volume would most likely be unresolved at this resolution and hence captured by the isotropic template.

Our discovery that the most massive halos in the local universe dominate the p - and d -wave constraints (running the inference using the ~ 20 largest halos gives constraints which differ by a factor only $\mathcal{O}(1)$ compared to the full result) raises the question of whether stronger constraints could be obtained using a dedicated cluster catalogue extending to higher redshift than CSiBORG. To address this we calculate the J factor produced by the Master Catalogue of X-ray Clusters (MCXC; [85]), a compilation of clusters detected through their X-ray-emitting gas.

We find that the total J factor of the CSiBORG catalogue is larger by factor of ~ 10 than that from MCXC. This is a result of the incompleteness of the MCXC catalogue as well as the various selection effects involved, which outweigh its larger redshift range and are absent from CSiBORG. The CSiBORG suite is therefore optimal in terms of its all-sky constraining power.

Nevertheless, since the p - and d -wave annihilation channels are strongly dependent on relative velocity of dark matter particles, and thus the total halo mass, it might still be worthwhile to explore constrained simulations with larger simulation volumes than CSiBORG to include the contributions from more distant massive halos. Further constraining power may be extracted from the angular dependence of the s -, p - and d -wave annihilation signals, which we do not fully exploit due to the relatively coarse resolution of our all-sky maps. Useful future work would therefore be to use higher-resolution simulations or observations of clusters to compare their predicted and observed flux profiles in greater detail. Note that the angular resolution of the *Fermi* data is approximately `nside` ≈ 1024 , so significant improvements in resolution are possible. The positions and masses of local dark matter clusters may be found in the public CSiBORG halo catalogues [52].

3. Cluster masses

As demonstrated in Fig. 4 and indicated by Baxter *et al.* [39], for p -wave and d -wave annihilation, the constraints on cross-section are dominated by the largest mass objects. It is therefore more important to correctly obtain cluster masses than it is when considering s -wave models [cf. Fig. 9 of 40]. In this work we have used the masses obtained from constrained N -body simulations, with initial conditions inferred using the BORG algorithm. This is an alternative to traditional estimates of cluster masses, which typically use one of the virial theorem [86], X-ray measurements [87], the Sunyaev Zel'dovich effect [88, 89] or weak lensing [90, 91]. These measurements tend to lead to significantly different measurements of masses for the same clusters [e.g. Fig. 3 of 92], so it is not clear whether these traditional methods offer a more appropriate route to obtaining J factor maps as each method would produce very different constraints.

It has been found that the halo mass function in CSiBORG is higher than the average Λ CDM expectation at the massive end [43]. Although cosmic variance is high in this regime, this still represents a $\sim 2\sigma$ effect. To determine the effect of this potential mass discrepancy, we obtain a single new posterior sample of the initial conditions with a different gravity model (using the COmoving Lagrangian Acceleration (COLA) method [93]), different time-stepping in the forward-model, a different method for generating power spectra (CLASS [94] instead of Eisenstein & Hu [95]) and a more robust likelihood [96], designed to remove the effects of unknown systematic uncertainties on scales larger than 1.4° . We then run a simulation with these initial conditions but otherwise identical to CSiBORG. This reconstruction produces 2- and 3-point statistics of the density field and a halo mass function which is closer to that expected from a random Λ CDM realisation. However, the re-simulated halo masses are systematically smaller than those observed and some objects (e.g. the Perseus cluster) are less prominent than in our fiducial reconstruction. These modifications to the older BORG algorithm are studied in more detail in [97].

Due to the variety of changes, this simulation is useful to test the robustness of our results to the reconstruction analysis. We produce J factor maps for this simulation and rerun the end-to-end inference. We find this new simulation produces weaker constraints than our fiducial analysis, with changes in the constraints of up to a factor of ~ 5 and ~ 12 for p - and d -wave, respectively. This is to be expected given the systematically smaller cluster masses obtained with the updated initial conditions and is much greater than the variation in constraints between CSiBORG realisations, which is typically $\sim 40 - 50\%$. We note that this variation is comparable to what one would obtain using measured clustered mass because different measurements give highly variable results [92]. It is the most significant uncertainty in our analysis.

4. Astrophysical templates

In our fiducial analysis, we use the latest galactic diffuse model provided by the Fermi Collaboration (g11_iem_v07). Although we find little degeneracy between the normalisation of the astrophysical templates and the amplitude of the J -factor maps (and hence a_ℓ constraints), we nonetheless re-run our inference using an older template (g11_iem_v02) to estimate the systematic effect of the choice of galactic template. As in Bartlett *et al.* [40], we find that the constraints usually weaken slightly when using the older model, by up to 24% for p -wave and up to 31% for d -wave, although at low m_χ the d -wave constraints can be up to 7% tighter with the older model. This variation is small compared to that caused by the cluster masses.

C. Thermal relics

In this work we have focused on dark matter particles of mass $2 - 500 \text{ GeV}/c^2$ since, if the thermally-average annihilation cross-section is $\langle\sigma v\rangle_{\text{th}} \approx 3 \times 10^{-26} \text{ cm}^3\text{s}^{-1}$ [98] and these particles are thermal relics, then the current abundance of dark matter is reproduced. This cross-section is comparable to the electroweak coupling of the Standard Model, motivating the study of these dark matter candidates. In fact, the previously quoted $\langle\sigma v\rangle_{\text{th}}$ is appropriate for s -wave annihilation only. Hence, in this section we extend the analysis of Steigman *et al.* [98] to obtain the equivalent values for p - and d -wave annihilation, and compare to the a_ℓ we obtain.

We assume that $\sigma v = a_\ell v^{2\ell}$ and that dark matter particles are non-relativistic and follow a Boltzmann distribution. The thermally-averaged cross-section at temperature T is then

$$\langle\sigma v\rangle = \frac{\int d^3k_1 d^3k_2 \exp\left(-\frac{E_1+E_2}{T}\right) \sigma v}{\int d^3k_1 d^3k_2 \exp\left(-\frac{E_1+E_2}{T}\right)} = \frac{4^\ell \Gamma\left(\ell + \frac{3}{2}\right) a_\ell}{\Gamma\left(\frac{3}{2}\right)} x^\ell, \quad (21)$$

where k_1 and k_2 are the phase-space momenta and $x = m_\chi/T$. One must then solve the equation governing the number density, n , of dark matter

$$\frac{dY}{dx} = \frac{s \langle\sigma v\rangle}{Hx} \left[1 + \frac{1}{3} \frac{d(\log g_s)}{d(\log T)} \right] (Y_{\text{eq}}^2 - Y^2), \quad (22)$$

where $Y = n/s$ for entropy density s , g_s is the number of relativistic degrees of freedom contributing to the entropy density, H is the Hubble parameter, and the equilibrium value of Y is

$$Y_{\text{eq}} = \frac{45}{2\pi^4} \left(\frac{\pi}{8}\right)^{1/2} \frac{g_\chi}{g_s} x^{3/2} \exp(-x), \quad (23)$$

where the dark matter particle has g_χ degrees of freedom. Since this is a numerically stiff differential equation, we follow Steigman *et al.* [98] and solve for $W = \log Y$ instead. We also take $g_s(T)$ from the calculations of

Laine and Schröder [99]. Using an implicit Runge-Kutta method of the Radau IIA family of order 5 [100], we solve from $x = 1$ to $x = 10^3$, with an initial condition set using the approximate solution [101]

$$Y(x) \approx \frac{x^{\ell+2}}{2\lambda} + Y_{\text{eq}}(x), \quad (24)$$

which is valid long before freeze-out, where $\lambda \equiv 2.76 \times 10^{35} m_\chi \langle \sigma v \rangle_0$ for $\langle \sigma v \rangle = \langle \sigma v \rangle_0 x^{-\ell}$ and where m_χ is in GeV and $\langle \sigma v \rangle_0$ is in $\text{cm}^3 \text{s}^{-1}$. We then convert our solution to a density parameter

$$\Omega_\chi = \frac{8\pi G}{3H_0^2} m_\chi s_0 Y_0, \quad (25)$$

where H_0 , s_0 and Y_0 are the values of H , s and Y evaluated today. By comparing this value to $\Omega_\chi h^2 = 0.11$ [102], for $H_0 = 100h \text{ km s}^{-1} \text{ Mpc}^{-1}$, we repeat the analysis for varying a_ℓ at fixed m_χ to obtain the thermal relic cross-section which reproduces the present-day dark matter abundance.

This is plotted in Fig. 5 as a function of m_χ for $\ell = 0, 1, 2$. We find that the required p -wave coefficient is $a_1 \sim (1-3) \times 10^{-25} \text{ cm}^3 \text{ s}^{-1}$, whereas for d -wave this is $a_2 \sim (4-9) \times 10^{-25} \text{ cm}^3 \text{ s}^{-1}$. In both cases, this is several orders of magnitude smaller than the constraints we find in Fig. 3, and thus we cannot rule out dark matter being a thermal relic with a velocity-dependent cross-section using large scale structure. These conclusions are consistent with those discussed in the context of the extragalactic gamma-ray background [103, 104]; a detection of a p -wave annihilation signal would suggest a non-thermal origin of the present-day dark matter abundance.

We note that approximate analytic solutions of Eq. (25) exist for p - and d -wave annihilation [e.g. 37, 105]. In these cases, if freeze-out occurs when $x = x_f$ and x_f is the same for all ℓ , then to obtain the p - and d -wave $\langle \sigma v \rangle_{\text{th}}$ from the s -wave analysis, one would multiply $a_{0,\text{th}}$ by $x_f/3 \approx 6.7$ and $x_f^2/20 \approx 20$, respectively, where we have used $x_f \approx 20$. These ratios give the dashed horizontal lines in Fig. 5, when multiplied by the fiducial value of $a_0 = 3 \times 10^{-26} \text{ cm}^3 \text{ s}^{-1}$.

D. Comparison to the literature

An attempt to combine the relic abundance requirements with the GCE and lack of detection in dwarf galaxies was proposed by Choquette *et al.* [106]. They suggested that a metastable particle undergoing s -wave annihilation can produce the thermal abundance of dark matter particles, and these daughter particles can then undergo p -wave annihilation in the present epoch. They find that a dark matter particle mass $m_\chi \sim 90 \text{ GeV}/c^2$ with an annihilation cross-section given by $a_1 \sim 10^{-20} \text{ cm}^3 \text{ s}^{-1}$ for the $b\bar{b}$ channel can reproduce the GCE and survive all other tests. For this mass and channel, the a_1 required to explain the GCE is ruled out at

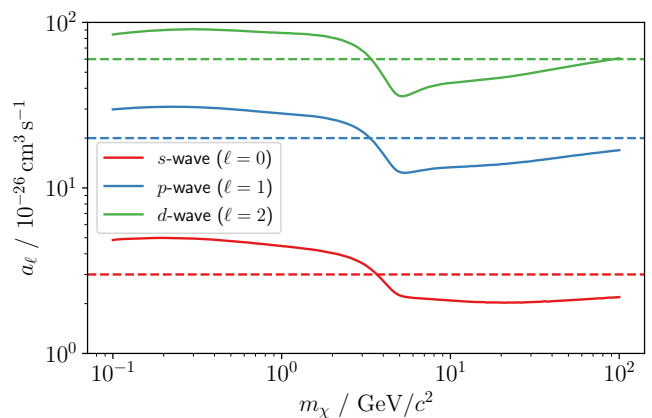


FIG. 5. Annihilation cross-section coefficient ($\sigma v = a_\ell (v/c)^\ell$) as a function of dark matter particle mass, m_χ , required to give a present-day dark matter abundance of $\Omega_\chi h^2 = 0.11$ for a thermal relic. We plot the results for s -, p - and d -wave annihilation and see that the required a_ℓ increases by less than an order of magnitude for a unit change of ℓ . The dashed horizontal lines give the standard value of $a_0 = 3 \times 10^{-26} \text{ cm}^3 \text{ s}^{-1}$ for s -wave, and this value multiplied by $x_f/3$ and $x_f^2/20$ for p - and d -wave, assuming a freeze-out value of x of $x_f = 20$.

over 1σ confidence in our analysis, suggesting that large scale structure disfavors this interpretation. In particular, they convert constraints on a_0 from clusters to constraints on a_1 by multiplying by multiples of the square of the velocity dispersion, and they find the Fornax cluster to be the most constraining object, with constraints which are ~ 2 orders of magnitude weaker than those given in Fig. 3. Since we perform a more careful analysis and obtain tight constraints on a_1 , future work should be dedicated to repeating the analyses cited by Choquette *et al.* [106] but with the correct velocity-dependent J factors.

If dark matter annihilated via the e^+e^- channel, then the resulting cosmic rays from the Milky Way could be detectable in Voyager 1 and the AMS-02 data. Boudaud *et al.* [78] considered this effect, and found constraints on p -wave annihilation for this channel which are tighter than our constraints, by up to approximately one order of magnitude (see Fig. 3). Their results are found to be robust to choice of profile used for the galactic halo, although are only applicable to the e^+e^- channel.

This is supported by Johnson *et al.* [107], who obtain a null detection of p -wave annihilation as the cause of the GCE, since they do not find a spike in emission around Sgr A*. Moreover, since s - and p -wave annihilation produce different spatial distributions of emission [63] for the same density profile, it is argued that, to explain the GCE, p -wave annihilation would require a slope of the density profile of the Milky Way much steeper than normally considered ($\gamma \sim 1.5-1.7$ compared to $\gamma \sim 1.2-1.4$ for s -wave) [108], further questioning whether velocity-dependent annihilation is the cause of this detection.

Alongside the GCE, one of the most common targets for indirect dark matter annihilation searches are dwarf galaxies in the Local Group due to their proximity and low baryon fraction. In Fig. 3 we compare our p -wave constraints to those obtained by these objects [76, 77, 109] for the $b\bar{b}$ channel, and find that our constraints are up to two orders of magnitude tighter. Similarly, we find that our d -wave constraints are approximately seven orders of magnitude tighter than those previously found from studying 25 dwarf spheroidal galaxies of the Milky Way [77], and hence lie outside the range of Fig. 3. This is in contrast to the results of s -wave annihilation, where dwarf galaxies give a constraint which is an order of magnitude tighter than that from large scale structure [40]. Assuming that clusters and dwarf galaxies have velocity dispersions of $\mathcal{O}(100)$ km s^{-1} and $\mathcal{O}(1 - 10)$ km s^{-1} , respectively, then one could estimate the p - and d -wave constraints by multiplying the s -wave ones by $\sigma^{2\ell}$. Given this ratio of velocity dispersions, one would anticipate that clusters can produce p - and d -wave constraints which are factors of 10^{2-3} and 10^{5-6} tighter, approximately as we find. Despite being less constraining for velocity-dependent annihilation, if one did detect such a signal, then dwarf galaxies could still have an important role, since each object would have the same spectrum, but the different density and velocity profiles would result in different spatial distributions of the signal, which one could use to determine ℓ [110].

If dark matter annihilated, then the energy injected into the intergalactic medium would modify the Universe's post-recombination ionisation history, and hence the observed cosmic microwave background (CMB). The large velocity dispersion in halos means that this is a predominantly low-redshift effect and could be detectable in the lowest multipoles of the CMB. Combining results from HST with BAO measurements, a joint analysis of data from Planck, WMAP9, ACT and SPT found no evidence of p -wave dark matter annihilation, ruling out cross-sections corresponding to $a_1 \sim 10^{-16} - 10^{-12}$ $\text{cm}^3 \text{s}^{-1}$ for the production of leptons at masses $m_\chi \sim 1 - 10^3$ GeV/c^2 at 95% confidence [111]. Our constraints are approximately four to five orders of magnitude more stringent than these results. One can similarly constrain dark matter annihilation via this process using the Lyman- α forest, but these constraints are also ~ 4 orders of magnitude weaker than those found in this work [112].

V. CONCLUSIONS

Annihilation of dark matter particles with velocity-dependent cross-sections can result in fluxes of gamma rays which are higher from extragalactic halos than from dwarf galaxies in the Local Group. In this work, we use the CSiBORG suite of constrained N -body simulations of the nearby Universe (within $155h^{-1}$ Mpc) to forward-model the expected emission from all halos down

to $M_{\text{vir}} = 4.4 \times 10^{11} M_\odot$ and therefore produce full-sky, field-level, energy-dependent intensity predictions for p -wave and d -wave dark matter annihilation. We combine these with templates describing emission by baryonic processes in the Milky Way, an isotropic background and point sources, and compare to observations from the *Fermi* Large Area Telescope. Marginalising over the amplitudes of these templates and uncertainties in the reconstructed dark matter density field, we find no evidence for velocity-dependent dark matter annihilation to any standard model particle.

We place upper limits on the annihilation cross-section as a function of dark matter particles mass, m_χ , in the range $m_\chi = 2 - 500$ GeV/c^2 and for different annihilation channels. For the $b\bar{b}$ channel, defining $\sigma v = a_\ell (v/c)^{2\ell}$ where $\ell = 1, 2$ for p and d -wave, respectively, we constrain $a_1 < 2.4 \times 10^{-21}$ $\text{cm}^3 \text{s}^{-1}$ and $a_2 < 3.0 \times 10^{-18}$ $\text{cm}^3 \text{s}^{-1}$ at 95% confidence for $m_\chi = 10$ GeV/c^2 . Our constraints are weaker for the e^+e^- channel, with $a_1 < 1.5 \times 10^{-20}$ $\text{cm}^3 \text{s}^{-1}$ and $a_2 < 1.9 \times 10^{-17}$ $\text{cm}^3 \text{s}^{-1}$ at 95% confidence for this particle mass. We find that these constraints are dominated by the most massive halos ($M_h \sim 10^{14-16} M_\odot$). Our constraints are four to five orders of magnitude more stringent than those on p -wave annihilation from cosmic microwave background analyses, and two (seven) orders of magnitude tighter than p -wave (d -wave) constraints from dwarf galaxies, as one would expect from the larger velocity dispersion in higher mass objects. Our bounds are however still several orders of magnitude above the value required to rule out dark matter being a thermal relic with a velocity-dependent annihilation cross-section.

In this work we have demonstrated the constraining power of the full halo field on velocity-dependent dark matter annihilation through a full-sky field-level inference, and obtained constraints which are several orders of magnitude tighter than alternative probes. Future work should be dedicated to higher-resolution inferences using the most constraining (highest mass) objects, incorporating other observations to constrain and marginalise over the density and velocity profiles, as well as investigating the case of Sommerfeld-enhanced annihilation channels as proposed in [60, 61].

The dominant systematic uncertainty in our analysis is the density field reconstruction (in particular its ability to reproduce high halo masses accurately), and hence future work should focus on understanding and improving this modelling (see [97]). Since anisotropic motions and baryonic processes can increase the J factor and hence the predicted signal, more precise modelling of these effects may achieve tighter constraints even with the same data.

DATA AVAILABILITY

This work required modifications to the CLUMPY package in order to model velocity-dependent dark matter

annihilation. These modifications will be included in a future CLUMPY release. Our J and D factor maps, which may be useful for other indirect detection analyses of current or future data, will be made available upon publication. As supplementary material on arXiv we provide the `Mathematica` notebooks used in deriving Eq. (A6).

ACKNOWLEDGMENTS

We thank Céline Combet, Sten Delos, Moritz Hütten, Jens Jasche, Eiichiro Komatsu, Guilhem Lavaux, David Maurin, Fabian Schmidt and Ewoud Wempe for useful discussions. We thank Jonathan Patterson for smoothly running the Glamdring Cluster hosted by the University of Oxford, where most of the data processing was performed.

AK acknowledges support from the Starting Grant

(ERC-2015-STG 678652) “GrInflaGal” of the European Research Council at MPA. DJB is supported by the Simons Collaboration on “Learning the Universe” and was supported by STFC and Oriel College, Oxford. HD is supported by a Royal Society University Research Fellowship (grant no. 211046). This project has received funding from the European Research Council (ERC) under the European Union’s Horizon 2020 research and innovation programme (grant agreement No 693024). This work was done within the Aquila Consortium (<https://www.aquila-consortium.org/>).

Some of the results in this paper have been derived using the HEALPY and HEALPIX [69, 70], CLUMPY [53–55], NUMPYRO [73, 74], NUMPY [113], SCIPY [114] and FERMIPY [71] packages.

For the purpose of open access, the authors have applied a Creative Commons Attribution (CC BY) licence to any Author Accepted Manuscript version arising.

-
- [1] L. Goodenough and D. Hooper, arXiv e-prints , arXiv:0910.2998 (2009).
 - [2] M. Ajello *et al.*, ApJ **819**, 44 (2016).
 - [3] T. Linden, N. L. Rodd, B. R. Safdi, and T. R. Slatyer, Phys. Rev. D **94**, 103013 (2016).
 - [4] D. Hooper and L. Goodenough, Physics Letters B **697**, 412 (2011).
 - [5] D. Hooper and T. Linden, Phys. Rev. D **84**, 123005 (2011).
 - [6] D. Hooper and T. R. Slatyer, Physics of the Dark Universe **2**, 118 (2013).
 - [7] B. Zhou *et al.*, Phys. Rev. D **91**, 123010 (2015).
 - [8] T. Daylan *et al.*, Physics of the Dark Universe **12**, 1 (2016).
 - [9] I. Cholis, Y.-M. Zhong, S. D. McDermott, and J. P. Surdutovich, arXiv e-prints , arXiv:2112.09706 (2021).
 - [10] R. J. J. Grand and S. D. M. White, MNRAS **511**, L55 (2022).
 - [11] K. N. Abazajian, J. Cosmology Astropart. Phys. **2011**, 010 (2011).
 - [12] R. M. O’Leary, M. D. Kistler, M. Kerr, and J. Dexter, arXiv e-prints , arXiv:1504.02477 (2015).
 - [13] J. Petrović, P. D. Serpico, and G. Zaharijas, J. Cosmology Astropart. Phys. **2015**, 023 (2015).
 - [14] S. K. Lee, M. Lisanti, B. R. Safdi, T. R. Slatyer, and W. Xue, Phys. Rev. Lett. **116**, 051103 (2016).
 - [15] M. Buschmann, N. L. Rodd, B. R. Safdi, L. J. Chang, S. Mishra-Sharma, M. Lisanti, and O. Macias, Phys. Rev. D **102**, 023023 (2020).
 - [16] A. Gautam *et al.*, arXiv e-prints , arXiv:2106.00222 (2021).
 - [17] D. Hooper, I. Cholis, T. Linden, J. M. Siegal-Gaskins, and T. R. Slatyer, Phys. Rev. D **88**, 083009 (2013).
 - [18] I. Cholis, D. Hooper, and T. Linden, J. Cosmology Astropart. Phys. **2015**, 043 (2015).
 - [19] R. K. Leane and T. R. Slatyer, arXiv e-prints , arXiv:1904.08430 (2019).
 - [20] K. N. Abazajian and M. Kaplinghat, Phys. Rev. D **86**, 083511 (2012).
 - [21] C. Gordon and O. Macías, Phys. Rev. D **88**, 083521 (2013).
 - [22] K. N. Abazajian, N. Canac, S. Horiuchi, and M. Kaplinghat, Phys. Rev. D **90**, 023526 (2014).
 - [23] F. Calore, I. Cholis, and C. Weniger, J. Cosmology Astropart. Phys. **2015**, 038 (2015).
 - [24] S. Horiuchi, M. Kaplinghat, and A. Kwa, J. Cosmology Astropart. Phys. **2016**, 053 (2016).
 - [25] J. Petrović, P. D. Serpico, and G. Zaharijaš, J. Cosmology Astropart. Phys. **2014**, 052 (2014).
 - [26] E. Carlson and S. Profumo, Phys. Rev. D **90**, 023015 (2014).
 - [27] I. Cholis, C. Evoli, F. Calore, T. Linden, C. Weniger, and D. Hooper, J. Cosmology Astropart. Phys. **2015**, 005 (2015).
 - [28] D. Gaggero, M. Taoso, A. Urbano, M. Valli, and P. Ullio, J. Cosmology Astropart. Phys. **2015**, 056 (2015).
 - [29] O. Macias, C. Gordon, R. M. Crocker, B. Coleman, D. Paterson, S. Horiuchi, and M. Pohl, Nature Astronomy **2**, 387 (2018).
 - [30] R. Bartels, E. Storm, C. Weniger, and F. Calore, Nature Astronomy **2**, 819 (2018).
 - [31] M. Ackermann *et al.*, Phys. Rev. Lett. **115**, 231301 (2015).
 - [32] A. Albert *et al.*, ApJ **834**, 110 (2017).
 - [33] V. Gammaldi *et al.*, Phys. Rev. D **104**, 083026 (2021).
 - [34] Y. G. Kim and K. Y. Lee, Phys. Rev. D **75**, 115012 (2007).
 - [35] K. Y. Lee, Y. G. Kim, and S. Shin, Journal of High Energy Physics **2008**, 100 (2008).
 - [36] J. Kumar and D. Marfatia, Phys. Rev. D **88**, 014035 (2013).
 - [37] F. Gacchino, L. Lopez-Honorez, and M. H. G. Tytgat, J. Cosmology Astropart. Phys. **2013**, 025 (2013).
 - [38] T. Toma, Phys. Rev. Lett. **111**, 091301 (2013).
 - [39] E. J. Baxter, J. Kumar, A. D. Paul, and J. Runburg, J. Cosmology Astropart. Phys. **2022**, 026 (2022).
 - [40] D. J. Bartlett, A. Kostić, H. Desmond, J. Jasche, and G. Lavaux, Phys. Rev. D **106**, 103526 (2022).
 - [41] D. J. Bartlett, H. Desmond, and P. G. Ferreira, Phys. Rev. D **103**, 023523 (2021).

- [42] H. Desmond, M. L. Hutt, J. Devriendt, and A. Slyz, *MNRAS* **511**, L45 (2022).
- [43] M. L. Hutt, H. Desmond, J. Devriendt, and A. Slyz, *MNRAS* **516**, 3592 (2022).
- [44] G. Lavaux and J. Jasche, *MNRAS* **455**, 3169 (2016).
- [45] J. Jasche and G. Lavaux, *Astron. Astrophys.* **625**, A64 (2019).
- [46] J. Jasche and B. D. Wandelt, *MNRAS* **425**, 1042 (2012).
- [47] J. Jasche and B. D. Wandelt, *MNRAS* **432**, 894 (2013).
- [48] J. Jasche, F. S. Kitaura, B. D. Wandelt, and T. A. Enßlin, *MNRAS* **406**, 60 (2010).
- [49] J. Jasche, F. Leclercq, and B. D. Wandelt, *J. Cosmology Astropart. Phys.* **2015**, 036 (2015).
- [50] R. Teyssier, *A&A* **385**, 337 (2002).
- [51] A. Bleuler, R. Teyssier, S. Carassou, and D. Martizzi, *Computational Astrophysics and Cosmology* **2**, 5 (2015).
- [52] M. L. Hutt, H. Desmond, J. Devriendt, and A. Slyz, “The effect of local universe constraints on halo abundance and clustering,” (2022).
- [53] A. Charbonnier, C. Combet, and D. Maurin, *Computer Physics Communications* **183**, 656 (2012).
- [54] V. Bonnivard, M. Hütten, E. Nezri, A. Charbonnier, C. Combet, and D. Maurin, *Computer Physics Communications* **200**, 336 (2016).
- [55] M. Hütten, C. Combet, and D. Maurin, *Computer Physics Communications* **235**, 336 (2019).
- [56] J. F. Navarro, C. S. Frenk, and S. D. M. White, *ApJ* **490**, 493 (1997).
- [57] F. Prada, A. A. Klypin, A. J. Cuesta, J. E. Betancort-Rijo, and J. Primack, *MNRAS* **423**, 3018 (2012), arXiv:1104.5130 [astro-ph.CO].
- [58] M. A. Sánchez-Conde and F. Prada, *MNRAS* **442**, 2271 (2014).
- [59] E. Piccirillo *et al.*, *J. Cosmology Astropart. Phys.* **2022**, 058 (2022).
- [60] G. Facchinetti, M. Stref, T. Lacroix, J. Lavalle, J. Pérez-Romero, D. Maurin, and M. A. Sánchez-Conde, arXiv e-prints, arXiv:2203.16491 (2022), arXiv:2203.16491 [astro-ph.CO].
- [61] T. Lacroix *et al.*, *J. Cosmology Astropart. Phys.* **2022**, 021 (2022).
- [62] E. L. Lokas and G. A. Mamon, *MNRAS* **321**, 155 (2001).
- [63] K. K. Boddy, J. Kumar, and L. E. Strigari, *Phys. Rev. D* **98**, 063012 (2018).
- [64] L. Osipkov, *Pisma v Astronomicheskii Zhurnal* **5**, 77 (1979).
- [65] D. Merritt, *The astronomical journal* **90**, 1027 (1985).
- [66] O. E. Gerhard, *Monthly Notices of the Royal Astronomical Society* **250**, 812 (1991).
- [67] B. Boucher, J. Kumar, V. B. Le, and J. Runburg, *Physical Review D* **106**, 023025 (2022).
- [68] J. Binney and S. Tremaine, *Galactic dynamics*, Vol. 13 (Princeton university press, 2011).
- [69] A. Zonca, L. Singer, D. Lenz, M. Reinecke, C. Rosset, E. Hivon, and K. Gorski, *Journal of Open Source Software* **4**, 1298 (2019).
- [70] K. M. Górski, E. Hivon, A. J. Banday, B. D. Wandelt, F. K. Hansen, M. Reinecke, and M. Bartelmann, *ApJ* **622**, 759 (2005).
- [71] M. Wood, R. Caputo, E. Charles, M. Di Mauro, J. Magill, J. S. Perkins, and Fermi-LAT Collaboration, in *35th International Cosmic Ray Conference (ICRC2017)*, International Cosmic Ray Conference, Vol. 301 (2017) p. 824.
- [72] F. Acero *et al.*, *ApJS* **223**, 26 (2016).
- [73] D. Phan, N. Pradhan, and M. Jankowiak, arXiv preprint arXiv:1912.11554 (2019).
- [74] E. Bingham *et al.*, *J. Mach. Learn. Res.* **20**, 28:1 (2019).
- [75] T. E. Jeltema and S. Profumo, *J. Cosmology Astropart. Phys.* **2008**, 003 (2008).
- [76] Y. Zhao, X.-J. Bi, H.-Y. Jia, P.-F. Yin, and F.-R. Zhu, *Phys. Rev. D* **93**, 083513 (2016).
- [77] K. K. Boddy, J. Kumar, A. B. Pace, J. Runburg, and L. E. Strigari, *Phys. Rev. D* **102**, 023029 (2020).
- [78] M. Boudaud, T. Lacroix, M. Stref, and J. Lavalle, *Phys. Rev. D* **99**, 061302 (2019), arXiv:1810.01680 [astro-ph.HE].
- [79] G. R. Blumenthal, S. M. Faber, R. Flores, and J. R. Primack, *ApJ* **301**, 27 (1986).
- [80] O. Y. Gnedin, A. V. Kravtsov, A. A. Klypin, and D. Nagai, *ApJ* **616**, 16 (2004).
- [81] A. Pontzen and F. Governato, *Mon. Not. Roy. Astron. Soc.* **421**, 3464 (2012).
- [82] A. Del Popolo and F. Pace, *Astrophys. Space Sci.* **361**, 162 (2016), [Erratum: *Astrophys.Space Sci.* 361, 225 (2016)], 1502.01947.
- [83] E. Board *et al.*, *J. Cosmology Astropart. Phys.* **2021**, 070 (2021).
- [84] D. McKeown *et al.*, *MNRAS* **513**, 55 (2022).
- [85] R. Piffaretti, M. Arnaud, G. Pratt, E. Pointecouteau, and J.-B. Melin, *Astronomy & Astrophysics* **534**, A109 (2011).
- [86] D. Merritt, *ApJ* **313**, 121 (1987).
- [87] A. E. Evrard, C. A. Metzler, and J. F. Navarro, *ApJ* **469**, 494 (1996).
- [88] R. A. Sunyaev and Y. B. Zeldovich, *Comments on Astrophysics and Space Physics* **2**, 66 (1970).
- [89] R. A. Sunyaev and I. B. Zeldovich, *ARA&A* **18**, 537 (1980).
- [90] H. Bonnet, Y. Mellier, and B. Fort, *ApJ* **427**, L83 (1994).
- [91] G. Fahlman, N. Kaiser, G. Squires, and D. Woods, *ApJ* **437**, 56 (1994).
- [92] S. Stopyra, H. V. Peiris, A. Pontzen, J. Jasche, and P. Natarajan, *MNRAS* **507**, 5425 (2021).
- [93] S. Tassev, M. Zaldarriaga, and D. J. Eisenstein, *J. Cosmology Astropart. Phys.* **2013**, 036 (2013).
- [94] D. Blas, J. Lesgourgues, and T. Tram, *Journal of Cosmology and Astro-Particle Physics* **2011**, 034 (2011).
- [95] D. J. Eisenstein and W. Hu, *ApJ* **496**, 605 (1998).
- [96] N. Porqueres, D. Kodi Ramanah, J. Jasche, and G. Lavaux, *A&A* **624**, A115 (2019), arXiv:1812.05113 [astro-ph.CO].
- [97] S. Stopyra, H. V. Peiris, A. Pontzen, J. Jasche, and G. Lavaux, “Towards accurate field-level inference of massive cosmic structures,” (2023), arXiv:2304.09193 [astro-ph.CO].
- [98] G. Steigman, B. Dasgupta, and J. F. Beacom, *Phys. Rev. D* **86**, 023506 (2012).
- [99] M. Laine and Y. Schröder, *Phys. Rev. D* **73**, 085009 (2006).
- [100] E. Hairer and G. Wanner, *Solving Ordinary Differential Equations II. Stiff and Differential-Algebraic Problems*, Vol. 14 (1996).
- [101] E. W. Kolb and M. S. Turner, *The Early Universe*, Vol. 69 (1990).

- [102] E. Komatsu *et al.*, ApJS **192**, 18 (2011).
 [103] S. Campbell, B. Dutta, and E. Komatsu, Phys. Rev. D **82**, 095007 (2010).
 [104] S. Campbell and B. Dutta, Phys. Rev. D **84**, 075004 (2011).
 [105] K. Griest and D. Seckel, Phys. Rev. D **43**, 3191 (1991).
 [106] J. Choquette, J. M. Cline, and J. M. Cornell, Phys. Rev. D **94**, 015018 (2016).
 [107] C. Johnson, R. Caputo, C. Karwin, S. Murgia, S. Ritz, J. Shelton, and Fermi-LAT Collaboration, Phys. Rev. D **99**, 103007 (2019).
 [108] K. Kiriū, J. Kumar, and J. Runburg, arXiv e-prints, arXiv:2208.14002 (2022).
 [109] Y. Zhao, X.-J. Bi, P.-F. Yin, and X. Zhang, Phys. Rev. D **97**, 063013 (2018).
 [110] E. J. Baxter, J. Kumar, A. B. Pace, and J. Runburg, J. Cosmology Astropart. Phys. **2021**, 030 (2021).
 [111] R. Diamanti, L. Lopez-Honorez, O. Mena, S. Palomares-Ruiz, and A. C. Vincent, J. Cosmology Astropart. Phys. **2014**, 017 (2014).
 [112] H. Liu, W. Qin, G. W. Ridgway, and T. R. Slatyer, Phys. Rev. D **104**, 043514 (2021), arXiv:2008.01084 [astro-ph.CO].
 [113] C. R. Harris *et al.*, Nature **585**, 357 (2020).
 [114] P. Virtanen *et al.*, Nature Methods **17**, 261 (2020).
 [115] H. Dejonghe, Phys. Rep. **133**, 217 (1986).

Appendix A: Calculation of J factor for d -wave

To calculate the d -wave J factor at a given distance from the halo centre, one needs to evaluate the corresponding fourth velocity moment at that distance, $\langle v^4 \rangle$. To do so, we assume ergodicity of the halo dark mat-

ter distribution function, which directly leads to the relation Eq. (12). However, this equation solves for the fourth moment of the radial velocity component, while we need the total $\langle v^4 \rangle$. One can show that in the case of an ergodic distribution function the following holds (see Problem 4.29 in [68] and Section 1.3 from [115])

$$\langle v_\theta^{n-j} v_\phi^{j-k} v_r^k \rangle = \langle v_r^n \rangle \frac{\Gamma(\frac{k+1}{2})\Gamma(\frac{n-j+1}{2})\Gamma(\frac{j-k+1}{2})}{\pi\Gamma(\frac{n+1}{2})}. \quad (\text{A1})$$

From this, the following relations directly follow

$$\langle v_\theta^4 \rangle = \langle v_\phi^4 \rangle = \langle v_r^4 \rangle \quad (\text{A2})$$

$$\langle v_\theta^2 v_\phi^2 \rangle = \langle v_\theta^2 v_r^2 \rangle = \langle v_\phi^2 v_r^2 \rangle = \frac{2}{3} \langle v_r^4 \rangle, \quad (\text{A3})$$

as does Eq. (13). Now, the only remaining issue is finding a solution to Eq. (12), since the second part of Eq. (11) can be directly obtained from Eq. (8). Note, that since we are assuming ergodicity, $\beta = 0$.

We assume NFW profiles (Eq. (7)) for our halos, which we rewrite as

$$\rho(s) = \frac{\rho_0}{cs(1+cs)^2}, \quad (\text{A4})$$

where c is the concentration, and $s = r/r_{\text{vir}}$. We can then solve Eq. (12) using Eq. (8). Noting that the gravitational potential in this notation is

$$\Phi(s) = -4\pi G \rho_0 r_s^2 \frac{\log(1+cs)}{cs}, \quad (\text{A5})$$

one obtains

$$\begin{aligned} \rho \langle v_r^4 \rangle = & \frac{4}{3} \pi^2 G^2 \rho_0^3 r_s^4 \left[-\frac{6(cs(cs(8cs+21)+6)-1)\log^2(cs+1)}{c^3 s^3} + \frac{6\text{Li}_2(c^2 s^2)(10cs+9\log(cs+1))}{cs} \right. \\ & - \frac{6\log(cs+1)}{c^2 s^2 (cs+1)} \left(cs(-3\pi^2(cs+1)+cs(3cs+35)+25) + 3cs(cs+1)\log(cs)+2 \right) \\ & + 288\text{Li}_3(cs+1) + \text{Li}_2(cs) \left(-\frac{108\log(cs+1)}{cs} - 120 \right) + 72\text{Li}_2(cs+1)(3-4\log(cs+1)) \\ & - \frac{52(\pi cs + \pi)^2 + 174cs + 177}{(cs+1)^2} + \frac{6}{cs(cs+1)^2} \\ & \left. + \frac{6(8cs+9)\log^3(cs+1)}{cs} + 72\log(cs)(3-2\log(cs+1))\log(cs+1) + 18\log(cs) \right] \\ & + \text{const}, \end{aligned} \quad (\text{A6})$$

where Li_2 and Li_3 represent the dilogarithm and trilogarithm, respectively. We use the implementations pro-

vided in the `polylogarithm` library⁶ to evaluate these. We impose $\lim_{s \rightarrow \infty} (\rho \langle v_r^4 \rangle)(s) = 0$, which fixes the inte-

⁶ <https://github.com/Expander/polylogarithm>

gration constant to 0. This is a consequence of the fact that the velocity dispersion itself goes to zero far away from the halo, for the case of ergodic phase-space distribution function which we assumed throughout for our halos. This in turn implies that the velocity distribution has a vanishing second moment and hence, by definition, the fourth moment is zero too in this limit.

This analytical solution was implemented within the CLUMPY package and tested against a numerical solution. For all our results regarding d -wave, we always utilise the analytical solution from Eq. (A6) and use the numerical solution only for cross-checking the results. We demonstrate the obtained J factor for d -wave in Fig. 1 obtained by substituting the expression from Eq. (A6) into

Eq. (11) and normalising by the total integrated J factor value and dividing by the corresponding quantity for s -wave (labelled as $\tilde{J}^{\ell=2}/\tilde{J}^{\ell=0}$). One sees that the shape of the angular distribution of the normalised J factor is qualitatively very similar to the $\beta = 0$, p -wave case and shows the same behaviour towards the halo centre and the edge of the halo.

Note that similar results have been obtained in Boddy *et al.* [63], who used Eddington inversion formula for obtaining the velocity moments. We chose to directly integrate the Jeans equations instead, since we were also interested in studying the anisotropic cases for the p -wave annihilation channel, and hence for consistency used the same approach for the d -wave J factor calculation.